Single and double ionization of helium in intense bicircular laser fields

Jan L Chaloupka

Department of Physics and Astronomy, University of Northern Colorado, Greeley, CO 80639, United States of America

E-mail: jan.chaloupka@unco.edu

Abstract

The single and double ionization of helium in intense $2\omega{:}\omega$ bicircular laser fields is analyzed with a classical ensemble method. A high-performance computational cluster is utilized to generate high-resolution data and to probe low-rate events. It is found that both counter- and co-rotating fields support rescattering and non-sequential double ionization (NSDI). The effects of scattering off of the ionic core are evident in the single-ionization energy spectra, and the role of the Coulomb potential is clearly visible in the electron momentum distributions. The dynamics of the double ionization processes are investigated by analyzing ionization phase, electron energy and momenta, and rescattering timing. For corotating fields, rescattering is only possible for ionization near the field minimum, placing limits on the efficiency of NSDI. For counterrotating fields, the electron trajectories that contribute to rescattering are found to fall into only three categories (looping, triangular, or a combination of the two), and the contributions from these trajectories is distinguishable in the resulting double-ion electron momentum distributions. This study explores the full range of field amplitude ratios that contribute to the dynamics of rescattering, and therefore provides an overall view of the limitations of using bicircular fields for applications in strong-field physics.

Keywords: strong-field physics, intense laser ionization, bicircular laser fields, classical ensemble simulations

(Some figures may appear in colour only in the online journal)

1. Introduction

In 1966, it was discovered that intense pulses from a ruby laser could be used to ionize xenon atoms [1]. In spite of the low photon energy compared to the atomic ionization potential, and counter to the traditional explanation of the photoelectric effect, it was found that ionization occurred readily, and that the ionization yield had a strong non-linear dependence on intensity. This phenomenon could be either explained by considering the simultaneous absorption of many photons, so-called multiphoton ionization, or with a classical view of the laser pulse, where the strong field distorts and suppresses the Coulomb barrier leading to tunnel ionization.

Years later, it was found that more than one electron could be liberated with a single pulse, leading to double ionization [2]. The observed double-ionization yield curves indicated that a more complex process, beyond simple tunnel ionization, was at work [3, 4]. Rather than mimicking the steep, monotonic rise of the single-ion yield curves, the double-ion curves exhibited an enhancement of several orders of magnitude over what was expected from sequential ionization, where single and double ionization would be considered to occur independently. It was clear that a form of non-sequential double ionization (NSDI) would be needed to describe the observed 'knee' of enhanced double ionization.

A simple semi-classical model known as rescattering was developed and has since been used for decades to help describe strong-field phenomena [5–8]. In this three-step process, a single electron is liberated via tunnel ionization through the laser-suppressed Coulomb barrier. After gaining kinetic energy in the oscillating laser field, it is driven back to the parent ion, where it may impact the ion and lead to double ionization.

Consequences of this mechanism have been observed experimentally with ion yield curves [3, 4], electron energy spectra [9] and ion and electron momentum distributions [10], and also with the observation of high-harmonic generation (HHG) [11–13].

Since the rescattering mechanism, and hence HHG and NSDI, rely on returning electron trajectories, these processes are most efficient for linear polarization, are reduced dramatically for increased ellipticity, and are typically absent for circular polarization [14]. But in 1995 it was observed that high-order harmonics could be generated with short pulses of two-color, circularly polarized light [15]. Here, the fundamental frequency of an ultrashort Ti:S laser was combined with its second harmonic, creating either counter- or co-rotating bicircular laser pulses. Efficient harmonic generation was observed with counterrotating fields, indicating a strong effect from returning electron trajectories. Since then there has been a great deal of theoretical and experimental work examining the interaction of bicircular pulses with atoms, most notably in the last few years [16–39].

In this paper, we present results from a large-scale classical ensemble simulation. By utilizing a high-performance computational cluster, a vast amount of data is generated across a broad set of conditions. The full range of the two-color field amplitude ratios that leads to rescattering is probed at high resolution, providing a complete look into the strong-field ionization of helium with bicircular pulses. Data that is experimentally accessible, such as ionization yield and electron energy and momentum, is presented alongside parameters that are not directly observable, such as ionization phase, rescattering timing, and electron trajectory patterns. The effect of the Coulomb potential is observed in the single ionization electron momenta, and double ionization yield, ionization phase, and electron energies are mapped out in great detail. Finally, various ionization pathways are connected to the resulting electron momentum distributions, showing how these processes can at least in part be discerned experimentally.

2. Methods

2.1. Classical ensemble

In this paper, and in our recent work [34], we employ a classical ensemble approach, where a completely classical model atom with a softened potential is used to simulate the atomic interaction with the laser pulse [34–48]. The Hamiltonian for this model atom is (in atomic units)

$$H = \frac{p_1^2}{2} + \frac{p_2^2}{2} - \frac{2}{\sqrt{r_1^2 + a^2}} - \frac{2}{\sqrt{r_2^2 + a^2}} + \frac{1}{\sqrt{r_{12}^2 + b^2}}, \quad (1)$$

where p_1 and p_2 are the electron momenta, r_1 and r_2 are the electron–ion distances, r_{12} is the distance between the electrons, and a and b are the softening parameters (equal to 0.825 and 0.10, respectively). The value of the a parameter is chosen such that the model atom is stable with the correct ground state energy, and the value of the b parameter is selected to

ensure strong e–e interaction while avoiding computational issues [48]. The classical ensemble technique is a natural fit for studying rescattering processes and has become widely adopted since its initial development in the 1990s.

As a purely classical technique, this method allows for excellent physical insight into strong-field processes, and complements the intuitive nature of the rescattering picture. In this work, we utilize a high-performance cluster to generate a large amount of computational data across a wide range of field parameters, allowing for the generation of high-resolution results and analysis of low-yield events. The number of simulation runs performed here far exceeds the typical classical ensemble study. For example, in our previous work [34], the results presented were produced from a total of $\sim 10^7$ events, while in this paper, roughly 10^{10} simulations runs were used. Where it was previously only possible to create individual curves of yield, energy, and timing information, we are now able to generate complete maps of these parameters, uncovering novel patterns of ionization dynamics.

2.2. Simpleman model

To help set the stage for the full results from our classical ensemble simulations, it is useful to first examine an elementary scenario. With the so-called 'simpleman' approach [25, 49–52], an electron is released into the field with zero initial kinetic energy, the effect of the Coulomb potential and electron–electron correlation is neglected, and pulse width effects are ignored. The well-known results from this model include the presence of returning trajectories for linear polarization (and their absence for circular polarization), and the observation of final electron energies ranging from zero to $2U_p$ (where U_p is the ponderomotive potential of a quivering electron in the laser field) depending upon the electron's release phase. The simpleman model also gives the final electron momenta as equal to the negative vector potential of the laser field at the time of electron release.

Figure 1 shows the electric field (black line), the negative vector potential (red line), and a simple electron trajectory (blue line) for several different field parameters. In all cases the field is composed of the fundamental frequency and its second harmonic, both with circular polarization, and rotating in opposite directions (counterrotating, lower sign below) or in the same direction (corotating, upper sign below), given by

$$E = \frac{E_0}{1+\beta} \cdot \begin{pmatrix} \cos(\omega t)\,\hat{y} - \sin(\omega t)\,\hat{x} \\ +\beta\,\cos(2\omega t)\,\hat{y} \mp \beta\,\sin(2\omega t)\,\hat{x} \end{pmatrix}. \quad (2)$$

With this definition, even when the $2\omega{:}\omega$ amplitude ratio (β) is varied, the peak electric field amplitude will remain fixed and equal to E_0. By taking the cycle average, the intensity is then given as

$$I = \frac{2(1+\beta^2)}{(1+\beta)^2} I_0, \quad (3)$$

where I is the true intensity of the bicircular field and I_0 is the intensity of single-color, linearly polarized light with the same peak amplitude E_0. We refer to I_0 as the 'normalized intensity', and this scaling convention is used throughout the paper. Since

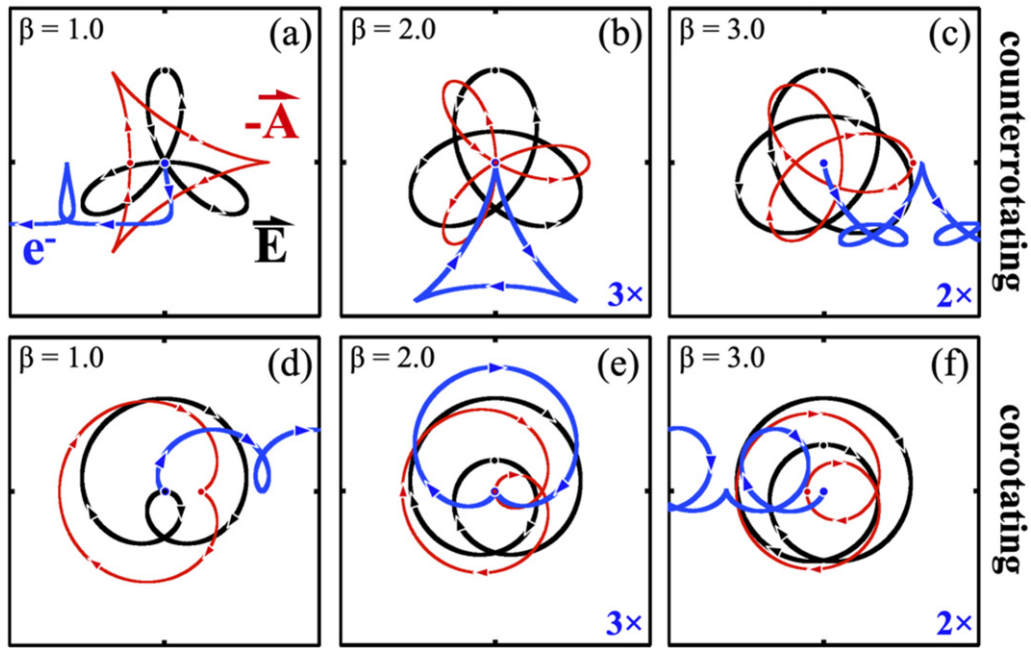J. Phys. B: At. Mol. Opt. Phys. **53** (2020) 185601

J L Chaloupka

Figure 1. Plots in the transverse plane of the electric field (black line), negative vector potential (red line), and the simpleman electron trajectory (blue line) are shown for (a)–(c) counterrotating and (d)–(f) corotating bicircular fields. The dot in each panel indicates the peak of the field for counterrotating fields, and the minimum of the field for corotating fields, and corresponds to the instant the electron is released into the field for the trajectory shown. For all cases the peak electric field amplitude is held fixed. The scales on the plots are arbitrary but consistent across all panels (the trajectory plots are magnified by a factor of three and two for the $\beta = 2.0$ and $\beta = 3.0$ cases, respectively).

the peak electric field amplitude is the same for a given normalized intensity, this allows for a direct comparison of ionization dynamics for all the field configurations presented in this article (for single-color fields with ellipticity ε, the scaling is given by $I = (1 + \varepsilon^2)I_0$).

In figures 1(a)–(c), a counterrotating field gives rise to three-fold symmetry in both the electric field pattern and the negative vector potential (and hence the expected electron momentum distribution), and results in a variety of interesting electron trajectories. The dot in the figures indicates the peak of the electric field, and is the instant that the electron is released into the field for the trajectory shown. For an amplitude ratio of $\beta = 2.0$ (figure 1(b)), a perfect triangular returning trajectory is observed. In figures 1(d)–(f), a corotating field is shown, giving rise to looping patterns, where the dot here indicates the field minimum. While for an amplitude ratio of $\beta = 2.0$ a returning trajectory is again observed, it will be unlikely to occur since ionization naturally peaks near the field *maximum*, and the electron shown here was released at the field *minimum*. This rudimentary analysis indicates that returning electron trajectories can exist for both counterrotating and corotating fields, but will occur at a significantly higher rate for counterrotating pulses.

3. Single ionization results

3.1. Electron energies

The most experimentally accessible forms of data in the study of strong-field physics are ionization yield curves and electron energy spectra. In fact, the observation of the dramatic

nonlinearity of the yield of Xe^+ as a function of laser intensity over 50 years ago [1] can be considered to mark the birth of intense laser–matter physics. But it was the observation of the electron energy spectra that gave significant insight into the actual processes at work [53]. The observation of a peak at zero energy and a drop-off to $2U_p$ is consistent with the release of an electron into the field for a range of phases, but peaked near the field maximum. And a high-energy tail extending to $10U_p$ is explained by considering elastic scattering of the electron off of the ion core.

In figure 2, electron energy spectra from our full simulation are presented. Here, and throughout the paper, a 10 fs pulse is focused to a 10 μm waist, and the model helium atom is located at the center of the focus [34]. The range of final electron energies allowed within the simpleman model is shown shaded and bound by dashed lines. For bicircular pulses, this energy range is identical for a given amplitude ratio for both counterrotating and corotating fields [25]. In fact, the final electron momentum, as predicted by the value of the negative vector potential, is exactly the same for counterrotating fields when the release phase is measured from the peak of the field, as it is for corotating fields when the phase is measured from the field minimum. A high-energy tail in the electron energy spectra is an indication of scattering off of the ion core, and is strongest in cases where returning electron trajectories are likely (linear polarization and counterrotating bicircular fields), weaker but still evident where returning trajectories are possible but less likely (corotating bicircular fields, in particular where $\beta = 2.0$), and absent where returning trajectories are not supported (elliptical and circular polarization).
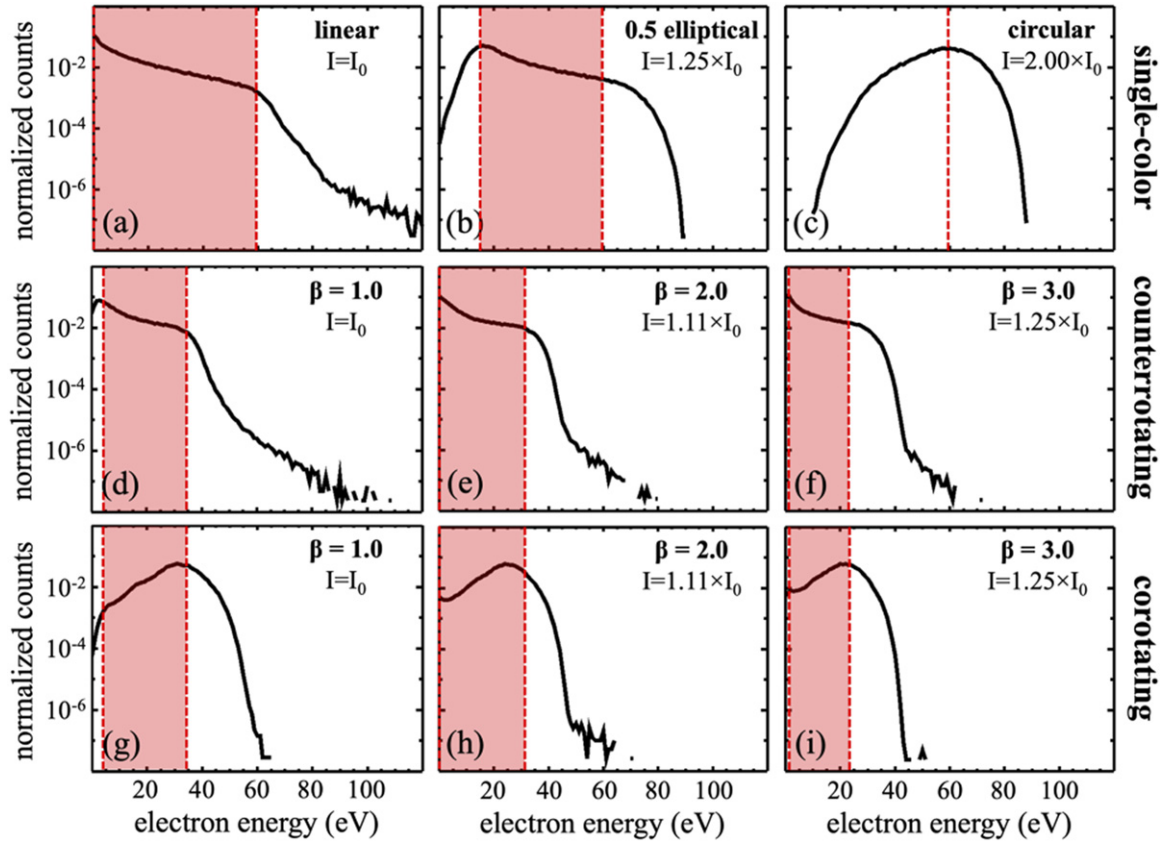
J. Phys. B: At. Mol. Opt. Phys. **53** (2020) 185601

J L Chaloupka

Figure 2. Single-ionization electron energy spectra for (a)–(c) 800 nm single-color pulses and 400:800 nm bicircular (d)–(f) counterrotating and (g)–(i) corotating fields are shown for a normalized peak intensity of 5×10^{14} W cm^{-2}. In all cases the peak electric field amplitude is set equal to the peak amplitude of the linearly polarized case (the scaling of the true intensity (I) in terms of the normalized intensity (I_0) is shown in each panel). The range of energies that is allowed under the simpleman model (for release at any phase) is indicated by the shaded regions. The vertical scale of each plot is normalized such that the area under the curve is equal to one. The horizontal scale in eV is the same for each plot and is shown at the bottom of the figure. Each plot is the result of 6×10^7 simulation runs.
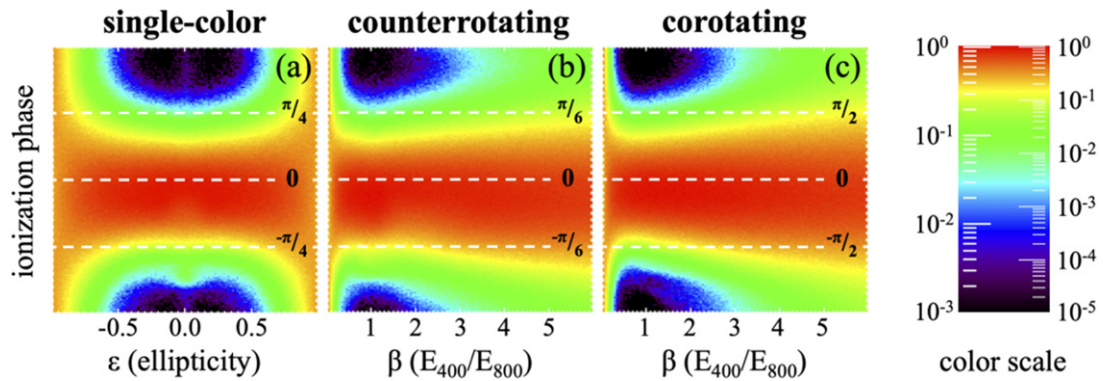

Figure 3. The single-ionization phase is shown for (a) single-color pulses as a function of ellipticity and for (b) counterrotating and (c) corotating fields as a function of the amplitude ratio β, all at a normalized peak intensity of 5×10^{14} W cm^{-2}. In all of the panels, the peak intensity occurs at the center line (zero phase), and the top and bottom of each panel correspond to an intensity minimum (the phase values are for 800 nm light). Each plot is the result of 3×10^7 simulation runs. Each panel is individually normalized to the peak value, and a logarithmic color scale is used (here the color scale that spans three orders of magnitude is used).

3.2. Ionization phase and electron momenta

Figure 3 shows a 'heat map' of the single ionization phase as a function of ellipticity for single-color pulses (figure 3(a)), and as a function of amplitude ratio β for counterrotating (figure 3(b)) and corotating (figure 3(c)) fields. Each panel is

independently normalized and the color indicates the relative likelihood of single ionization occurring for a range of phases with respect to the peak of the field. In each panel the center line indicates an intensity peak, and the top and bottom of the panel are an intensity minimum. This time scale is different for the three cases, and in terms of 800 nm light, this gives
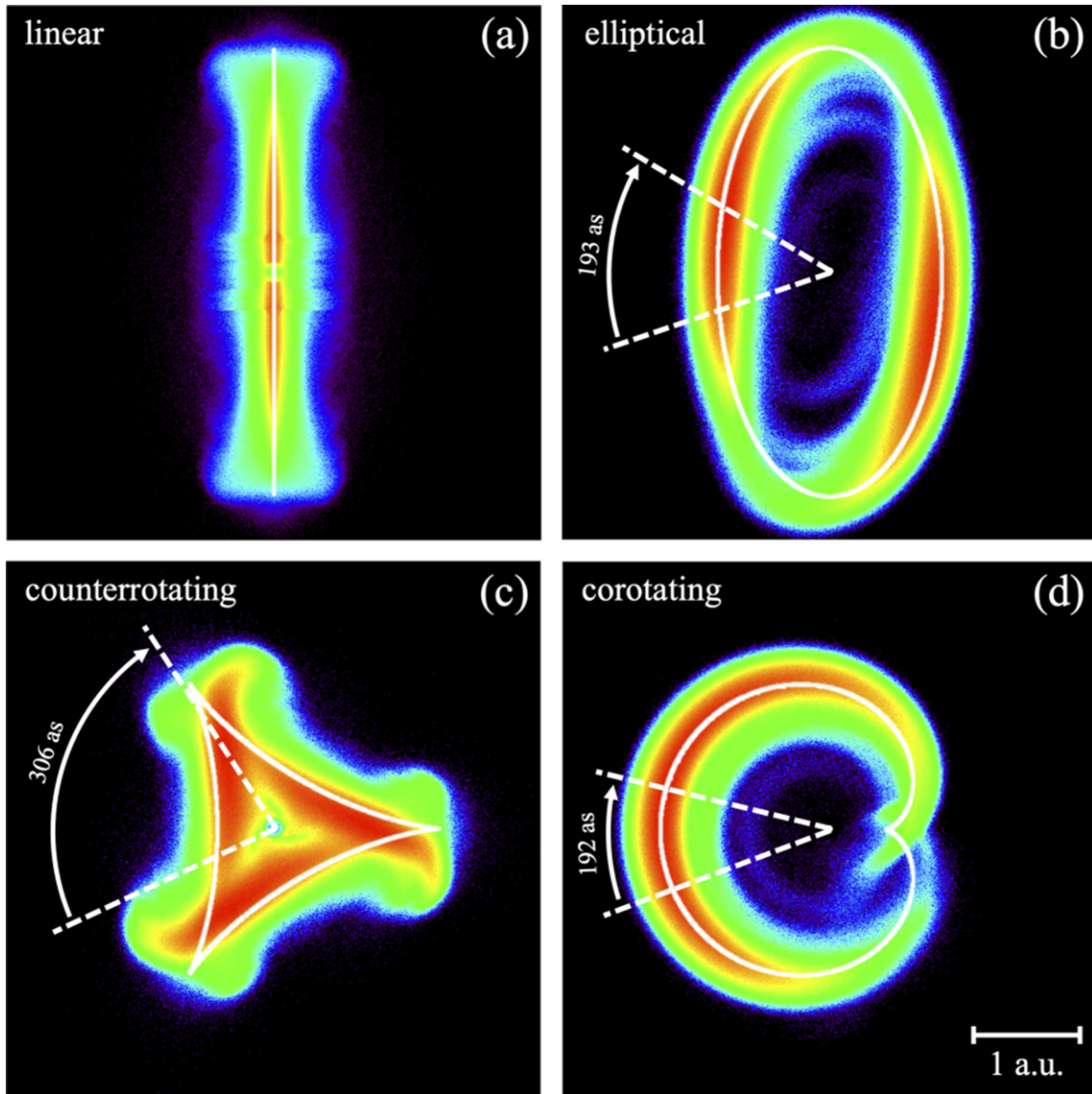
Figure 4. The transverse electron momenta for (a) linear and (b) elliptical ($\varepsilon = 0.5$) pulses, and for bicircular ($\beta = 1.0$) (c) counterrotating and (d) corotating fields are shown for a normalized peak intensity of 5×10^{14} W cm^{-2}. Superimposed on the color map is the negative vector potential corresponding to the peak intensity, indicating the shape of the momentum distribution expected from the simpleman model. For elliptical and bicircular fields, the ionization time is imprinted onto the two-dimensional momentum distributions, and in all cases there is a shift from the peak of ionization (lower dashed line) to the peak of the momentum distribution (upper dashed line). The momentum scale is shown in atomic units, and each panel is the result of 6×10^7 simulation runs. The color scale spans three orders of magnitude.

a peak-to-peak phase of π for single-color pulses, $2\pi/3$ for counterrotating fields, and 2π for corotating fields. In all cases the ionization peaks near the field maximum, indicating that the shape of the field distribution does not have a significant effect on when ionization occurs.

The ionization phase is not directly accessible by experiment, but it is imprinted onto the transverse electron momentum distribution. In figure 4, the momentum distributions are plotted for linear, elliptical, and bicircular pulses. The white line indicates the shape of the negative vector potential at the peak field intensity, showing a surprisingly strong match between the full simulation results and the predications of the simpleman model. For elliptical polarization and counter- and co-rotating bicircular fields, the spread of the

momentum distribution throughout the transverse plane allows for straightforward access to ionization timing information.

In figures 4(b)–(d), the electron momentum predicted by the simpleman model is compared to the peak of the observed electron momentum. The lower dashed line corresponds to the final momentum of an electron released at the most likely ionization phase, as predicted by the simpleman model. This is equal to the value of the negative vector potential at the peak of the ionization distribution, and since single ionization is at a maximum before the peak of the pulse, this results in a counter-clockwise rotation of the electron momentum direction. The upper dashed line corresponds to the maximum of the observed momentum distribution heat maps shown in figure 4. If our simulations dutifully obeyed the simpleman
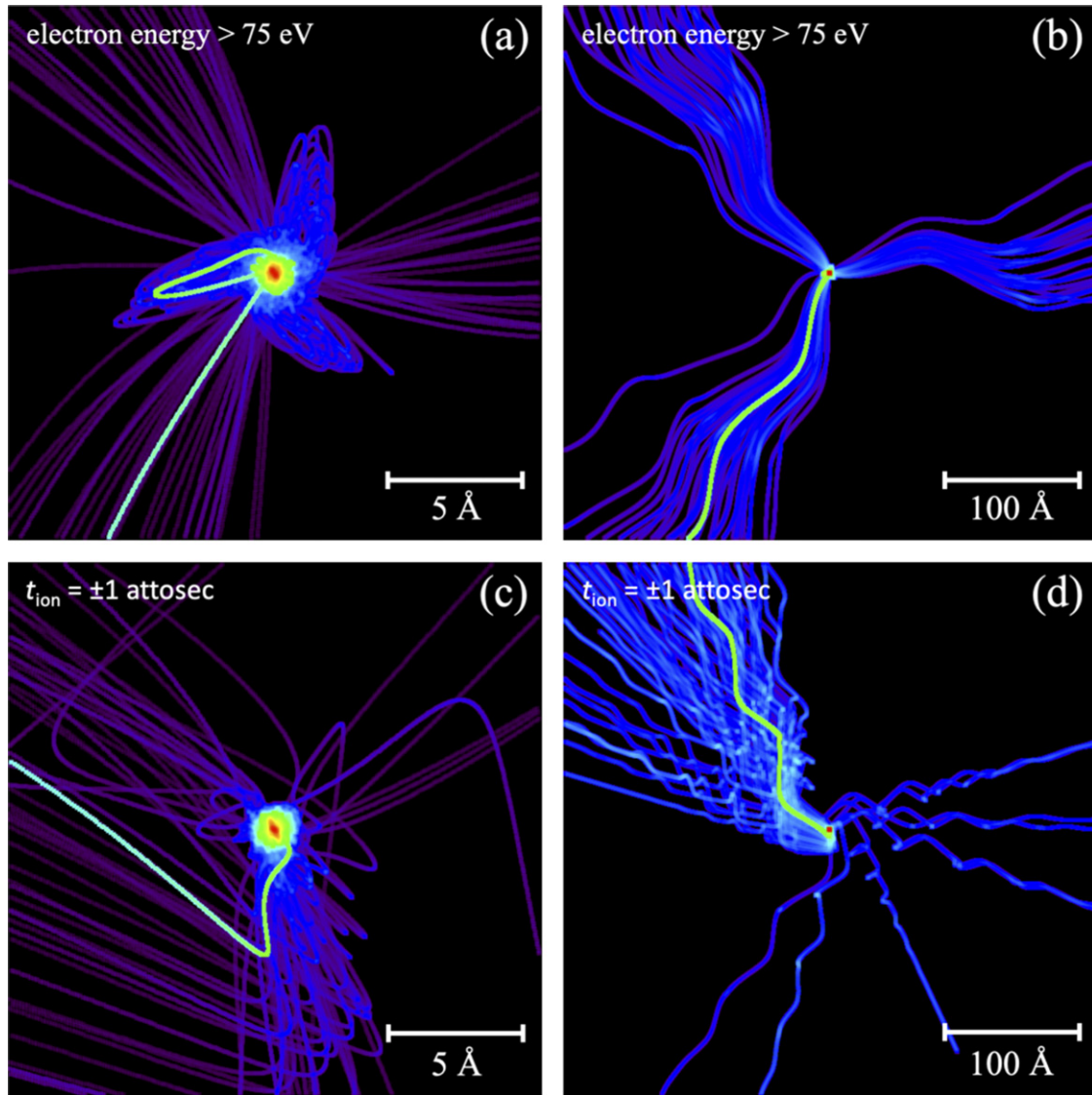
Figure 5. Ensembles of 100 electron trajectories are shown as a heat map for a $\beta = 1.0$ counterrotating pulse at 5×10^{14} W cm^{-2}. Simulation runs resulting in (a) and (b) high-energy electrons (>75 eV) show how scattering off of the parent ion is essential to produce energetic electrons. Simulation runs (c) and (d) where ionization occurs very near to the peak of the laser field (within one attosecond) show how dramatically the Coulomb interaction affects the trajectories. A single sample trajectory is highlighted for each case, and the trajectories are shown for each case at two different length scales. The color scale is optimized to highlight the trajectories in each plot.

model, these two lines would coincide. But the dramatic separation between what is expected from the simpleman model, and what is observed in the momentum distributions, is a fully classical manifestation [46] of an 'attoclock' delay due to the interaction of the freed electron with the Coulomb potential. Not surprisingly, this delay is largest for the counterrotating field, where electron trajectories are in general located closer to the ion core. This approach has been used to experimentally measure electron tunneling times [54–56], but a recent study has indicated that this time is nearly instantaneous, and that the observations of a rotation in the momentum distributions are due only to the effect of the Coulomb potential [57].

Both the generation of high-energy electrons and the effective delay of electron emission are a result of electron interaction with the parent ion. These phenomena can be visualized

by plotting the trajectories for a small ensemble of electrons corresponding to each case. In figures 5(a)–(b), an ensemble of 100 simulation runs that give final electron energies greater than 75 eV is shown, indicating how a short looping rescattering trajectory is necessary to generate high final electron energies. In figures 5(c)–(d), only trajectories for ionization very near the peak of the field are shown. For these cases, the simpleman model predicts a trajectory as shown in figure 1(a), resulting in a final drift directly to the left of the figure. But the potential of the parent ion significantly delays and distorts this path, resulting in a final drift to the upper left, as would be expected from a release into the field at a later time.

So just as the observation of energetic electrons liberated by linearly polarized light is an indication of a strong interaction with the ion core, a high-energy tail in the electron energy
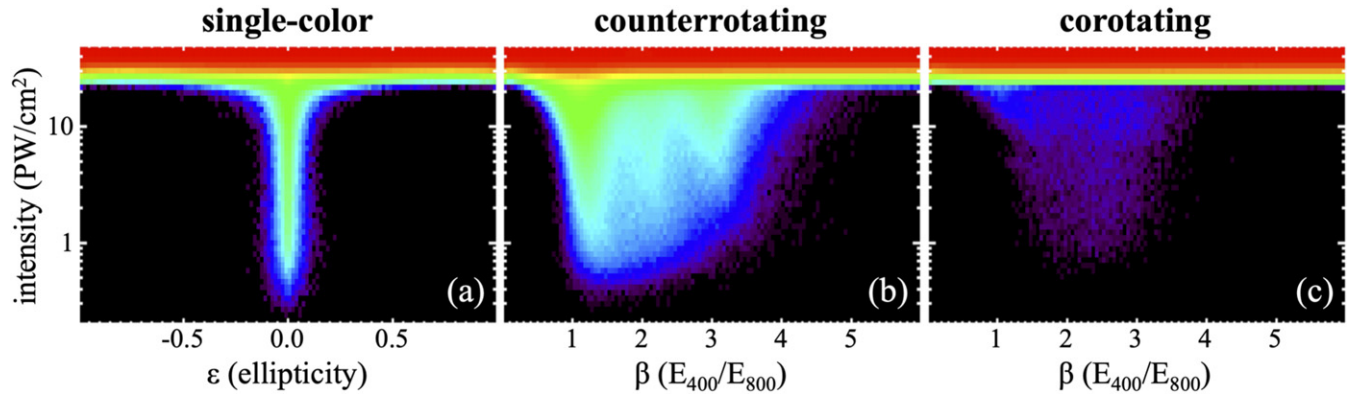
Figure 6. The double-ionization yield is shown for (a) single-color pulses as a function of ellipticity and for (b) counterrotating and (c) corotating fields as a function of the amplitude ratio β, for a range of intensities. In all cases, the yield saturates at the same normalized intensity and each plot exhibits a non-sequential ionization 'knee'. As expected for (a) single-color light, NSDI is limited to linear or mildly elliptical pulses, while for (b) counterrotating fields NSDI spans a wide range of field amplitude ratios. Remarkably, NSDI is present, albeit at much lower yields, across a wide range of ratios even for (c) corotating fields. The plots are a result of (a) 6×10^8, (b) 1.2×10^9, and (c) 1.2×10^9 simulation runs. The color scale spans five orders of magnitude.

spectra with bicircular fields is a clear indication of rescattering. But with bicircular fields there is an even more powerful and sensitive measure of this effect, namely, the observable effect on the final transverse electron momenta.

The single ionization results presented here are consistent with the established framework of ionization in single-color fields, and offer a natural introduction to the analysis of double ionization presented in the next section.

4. Double ionization results

4.1. Double ionization yield

Since the original observation of enhanced double ionization in 1983 [2], the 'knee' in the double ion yield curves [3, 4] has been an iconic result in strong-field physics. This is normally plotted as a simple yield vs intensity plot, but since we have access to a large data set spanning both pulse intensity and bicircular field shape (in the form of the 2ω:ω amplitude ratio) we present the double ionization yield as a heat map as a function of both the normalized intensity and the amplitude ratio. Single-color results are presented as a function of intensity and ellipticity.

In figure 6(a), the single-color maps show how NSDI diminishes rapidly as a function of increasing ellipticity. For counterrotating fields, the NSDI knee spans a broad range of amplitude ratios, as shown in figure 6(b). So even though the simpleman model predicts that perfect returning electron trajectories only occur for $\beta = 2.0$, it is clear that counterrotating fields support rescattering across a wide range of amplitude ratios. Finally, figure 6(c) shows that a broad region of NSDI exists even for corotating fields, but at a yield of roughly two orders of magnitude lower than the counterrotating case. An analysis of ionization phase, final electron energies and momenta, rescattering timing, and classical electron trajectories is presented in this section to help understand the processes that contribute to NSDI in counter- and corotating fields.

4.2. Ionization phase

The phase of the field at the instant that the first electron is freed for double ionization events is shown in figures 7(a)–(c). For single-color pulses, the ellipticity is varied from 0.0 to 0.3, but double ionization falls off significantly past 0.1, and is altogether absent at the highest ellipticities. For bicircular fields, the amplitude ratio β is varied across the full range of 0.0 to 6.0, but double ionization is absent for the lowest and highest values of β. In contrast to the single ionization case, the phase varies significantly for different field parameters. For single-color fields of varying ellipticity, the phase is broadly centered at the peak of the field (figure 7(a)). Since ionization naturally peaks near the field maximum, it is not surprising that pulses with linear or mildly elliptical polarizations result in a strong NSDI signal.

For counterrotating fields, the phase distribution exhibits interesting structure (figure 7(b)), indicating that trajectories that contribute to rescattering are sensitive to release phase. For example, for $\beta = 1.0$ pulses, electrons released after the peak of the pulse are more likely to result in NSDI, while for $\beta = 3.0$ pulses, electrons released slightly before the peak of the pulse are more likely to lead to rescattering. Since the double ionization phase distribution is a narrower subset of the single ionization distribution, the overall NSDI signal will be reduced.

For corotating fields, the situation is even more extreme, as electrons need to be released very late relative to the field maximum in order to lead to rescattering (figure 7(c)). This is what was expected from the simple analysis in the introduction, where electrons released at the field minimum could lead to returning trajectories for corotating fields. Since this is an unlikely ionization phase, it results in a much weaker NSDI signal.

4.3. Electron energies

While ionization phase is not directly measured experimentally, the final energy of electrons produced in the double
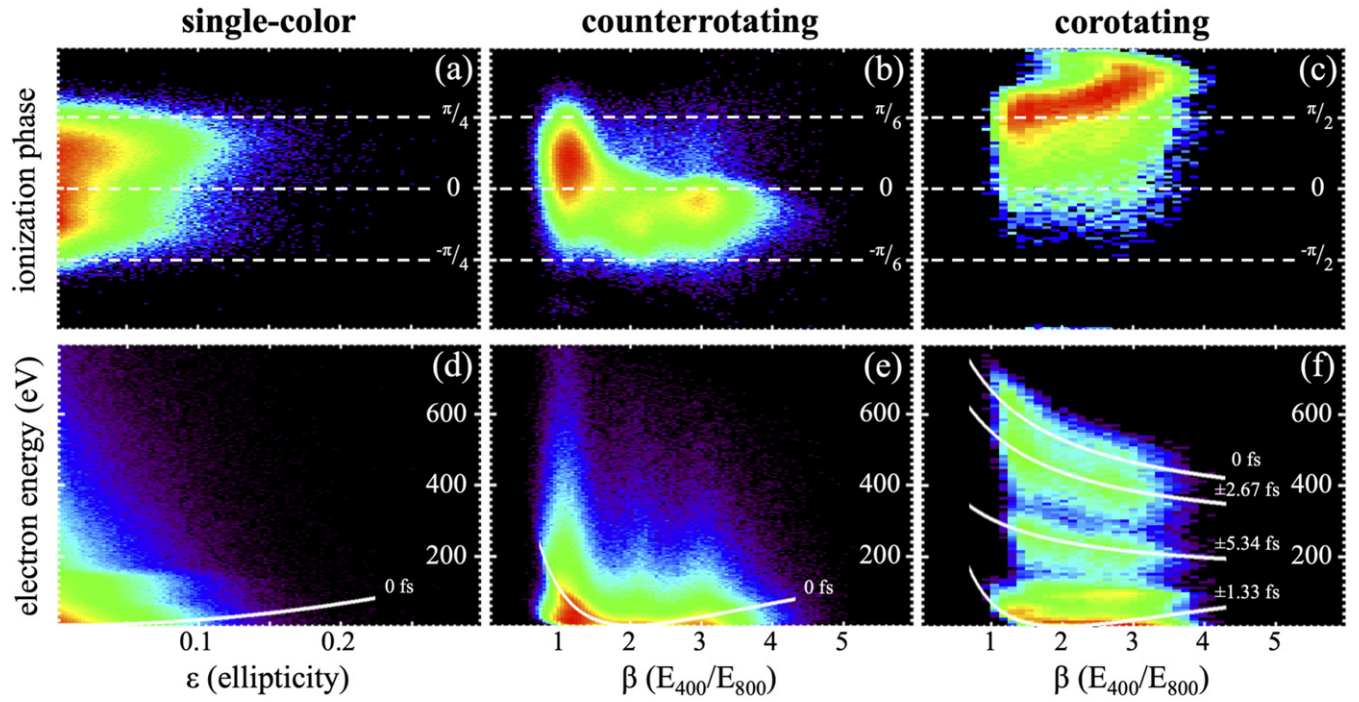
Figure 7. The (a)–(c) release phase for the first liberated electron and the (d)–(f) final electron energies for both electrons involved in double ionization are shown for (a) and (d) single-color pulses as a function of ellipticity and for (b) and (e) counterrotating and (c) and (f) corotating fields as a function of the amplitude ratio β, all at a normalized intensity of 1×10^{16} W cm^{-2}. The phase for (a) single-color pulses is centered at the peak of the field, but for (b) counterrotating fields the phase varies as a function of amplitude ratio. For (c) corotating fields, the release phase occurs well past the peak of the field. The (d)–(f) electron energies are in general the result of release into the field at the optimum phase for returning trajectories, smearing of energies due to impact ionization, and release near the field maximum due to field ionization after excitation. The energies expected from the simpleman model for electron release at different times are shown as white lines. The plots are a result of (a) and (d) 3.6×10^8, (b) and (e) 3.6×10^8, and (c) and (f) 1.92×10^9 simulation runs, and the color scale spans three orders of magnitude.

ionization process can be readily observed with coincidence techniques [9]. In figure 7(d) the final electron energies are shown for a single-color pulse as a function of ellipticity. The expected energies based on the simpleman model are indicated for release at the peak of the field. For low ellipticities, where measurable NSDI occurs, electron release at the field maximum would always result in very low electron energies, but rescattering significantly 'smears' the final energies to higher values. As expected, this is most apparent with linear polarization where rescattering is the strongest. For counterrotating bicircular fields, shown in figure 7(e), the energies are spread out both from the effects of rescattering, and from the non-zero value of the vector potential at the field maximum. This is most noticeable near the amplitude ratio of 1.0, where the vector potential is rather large at the time of the peak of the electric field.

But the most interesting case occurs with corotating fields. Here, electrons must be liberated near the field minimum in order to drive NSDI, and should result in low final electron energies. This is expected from the analysis of the simple returning trajectories shown in figure 1, and the resulting low-energy electrons are seen in figure 7(f). In cases where rescattering leads to impact excitation, the electrons subsequently liberated by field ionization will be most likely to be released near the field maximum and will take on higher energies.

This clear separation between electrons released via rescattering versus those that have been field ionized is a unique feature of corotating fields, and is clearly discernible in our results.

4.4. Electron momenta

In addition to recording ion yield curves and electron energy spectra, it has become commonplace for experimentalists to acquire the two-dimensional transverse electron momentum distributions resulting from double ionization [10, 28]. In figures 8(a)–(c) we present single-color results for linear and elliptical polarization, where the electrons are primarily distributed along the major polarization axis.

For counterrotating fields, shown in figures 8(d)–(f), the three-fold symmetric patterns expected from the shape of the vector potential are evident, but they are significantly smeared out from the effects of rescattering, and for corotating fields, shown in figures 8(g)–(i), the patterns exhibit spiral patterns.

The scale for all of the panels is shown in figure 8(g), and the normalized peak intensity is equal to 1×10^{16} W cm^{-2} in all cases. While these patterns may appear to be simply spread-out versions of the distributions expected from the negative vector potential, the contributions from different forms of double-ionization dynamics can be extracted from these distributions.
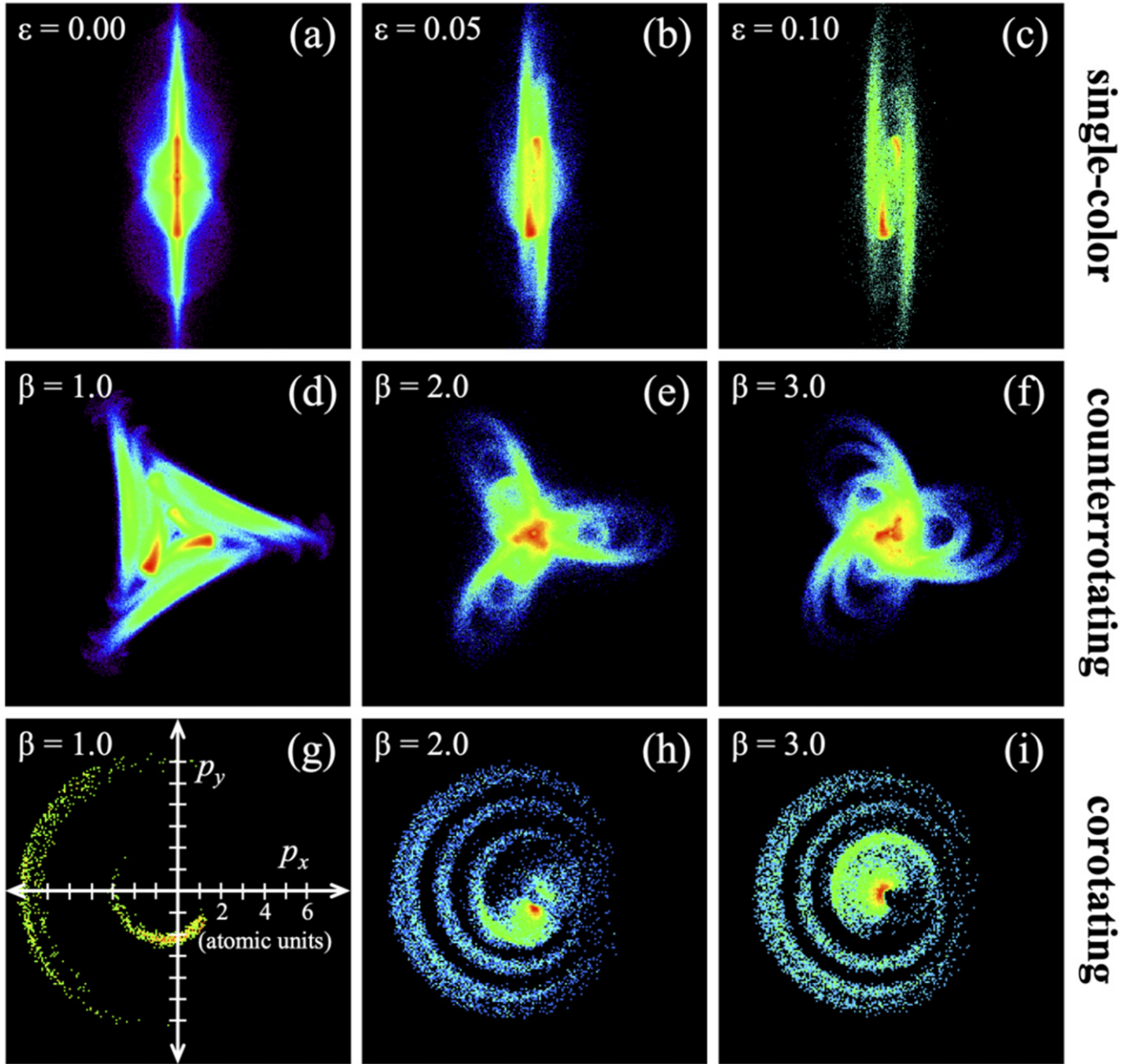
Figure 8. Transverse electron momenta for both electrons from double ionization events are shown for (a)–(c) single-color pulses and bicircular (d)–(f) counterrotating and (g)–(i) corotating fields, all at a normalized peak intensity of 1×10^{16} W cm^{-2}. For (a) linear polarization, the momentum distribution lies predominantly along the polarization direction, while for (b) and (c) elliptical polarization, the distributions begin to spread out along the minor axis. For both (d)–(f) counterrotating and (g)–(i) corotating fields, the momentum distributions are spread throughout the transverse plane, roughly in the patterns of the vector potential. The scale used for all of the panels is shown in (g), with momenta in atomic units. Each panel is the result of 1.2×10^8 simulation runs and the color scale spans three orders of magnitude.

4.5. Impact and excitation ionization

An analysis of the effect of the first and second electron liberated by either impact or excitation ionization is shown for counterrotating and corotating fields in figures 9 and 10, respectively. An impact ionization event is defined as the liberation of the second electron immediately following rescattering (when the second electron gains positive total energy less than 0.1 fs after the time of nearest return of the first freed electron), while excitation ionization occurs when the release

of the second electron is delayed, being the result of impact excitation followed by subsequent field ionization.

In figures 9(a) and (b), the pattern from a $\beta = 2.0$ counterrotating pulse (same as in figure 8(e)) shows how electrons involved in impact ionization exhibit a broad distribution due to the dispersive effects of rescattering. The momentum pattern for the first liberated electron (figure 9(a)) also shows a dip for low momenta, since returning electrons with very low energies will not lead to immediate impact ionization. The pattern
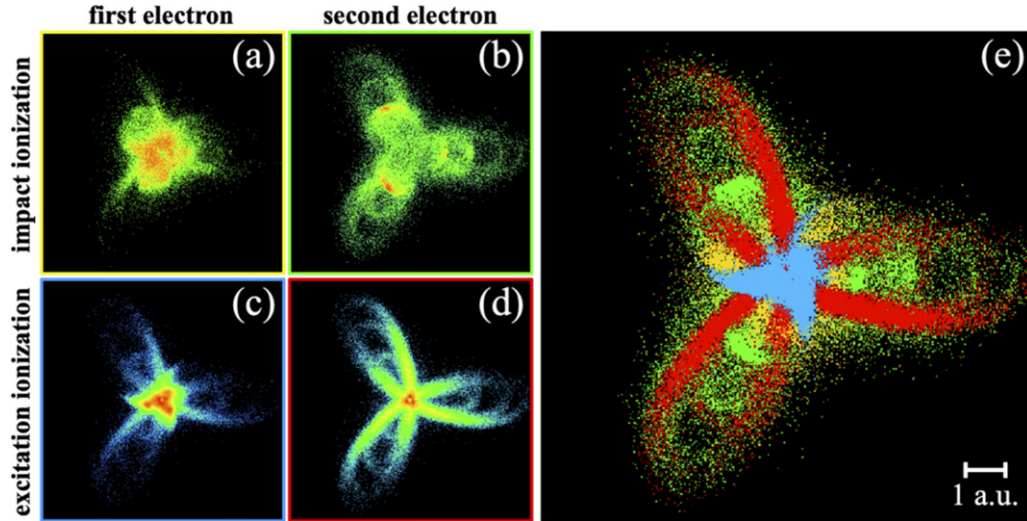
Figure 9. Transverse electron momenta are shown for a $\beta = 2.0$ counterrotating pulse at 1×10^{16} W cm^{-2} (as in figure 8(e)). The (a) first freed electron and the (b) second electron from impact ionization (double ionization occurring less than 0.1 fs after the nearest return of the first electron) events have smeared out momentum distributions. The distribution for the (c) first electron contributing to impact excitation and subsequent field ionization is peaked at low momenta, and the pattern from the (d) second, field-ionized, electron takes on the shape of the vector potential. Contributions from these four patterns are color coded and (e) combined into a single image. Here, the composite pattern takes on the color for the most likely process at each location in the distribution. This figure is the result of 1.2×10^8 simulation runs, the color scale spans three orders of magnitude (for (a)–(d)), and the scale is displayed in atomic units.
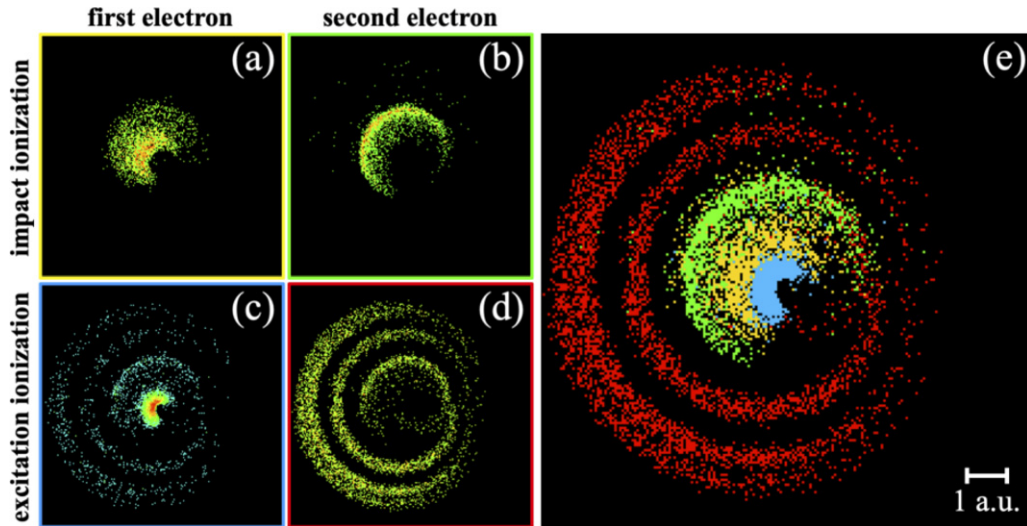

Figure 10. Transverse electron momenta are shown for a $\beta = 3.0$ corotating pulse at 1×10^{16} W cm^{-2} (as in figure 8(i)). The (a) first freed electron and the (b) second electron from impact ionization events have smeared out momentum distributions. The distribution for the (c) first electron contributing to impact excitation and subsequent field ionization is peaked at low momenta, and corresponds to electrons released near the field minimum and returning to the ion with low energies. The pattern from the (d) second, field-ionized, electron takes on the shape of the vector potential, and since this electron is released near the peak of the field, it is well separated from the rest of the momentum distribution. Contributions from these four patterns are color coded and (e) combined into a single image. This figure is the result of 1.2×10^8 simulation runs, the color scale spans three orders of magnitude (for (a)–(d)), and the scale is displayed in atomic units.

for the second electron (figure 9(b)) consists of defined peaks corresponding to the impact timing amid a broad distribution loosely following the vector potential pattern.

For electrons involved in excitation ionization, shown in figures 9(c) and (d), the patterns are significantly different. The first electron returns with relatively low energy, enough to drive excitation of the second electron, but not enough to lead directly to impact ionization. The second electron is released

through field ionization, and, not surprisingly, the momentum distribution nicely takes on the shape of the vector potential.

A composite image generated from these four patterns is shown in figure 9(e). Here, the color indicates the most likely process that contributes to the electron momentum for that location in the plot. Yellow and green represent the first and second electron from impact ionization, and blue and red represent the first and second electron from excitation
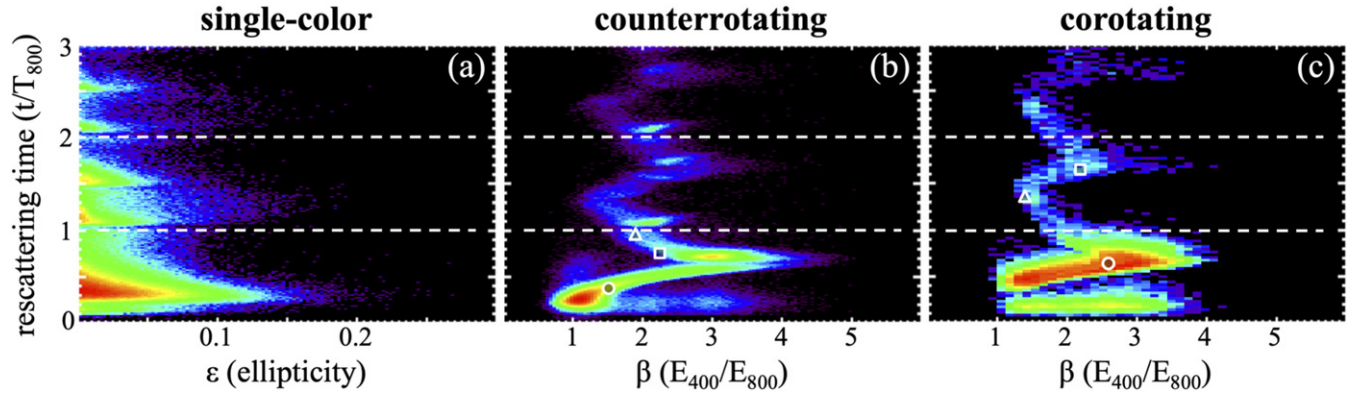
Figure 11. The rescattering timing, defined as the difference between the single ionization time and the subsequent time of nearest return, is shown for (a) single-color pulses as a function of ellipticity and for (b) counterrotating and (c) corotating fields as a function of the amplitude ratio β, all at a normalized peak intensity of 1×10^{16} W cm^{-2}. A sub-cycle return time is most likely in all cases, but multiple returns are possible, provided that the field supports closed-loop trajectories. This is possible for release near the peak of the field for linear polarization or $\beta = 2.0$ counterrotating fields, and for release near the field minimum for $\beta = 2.0$ corotating fields. The plots are a result of (a) 3.6×10^8, (b) 3.6×10^8, and (c) 1.92×10^9 simulation runs, and the color scale spans three orders of magnitude.
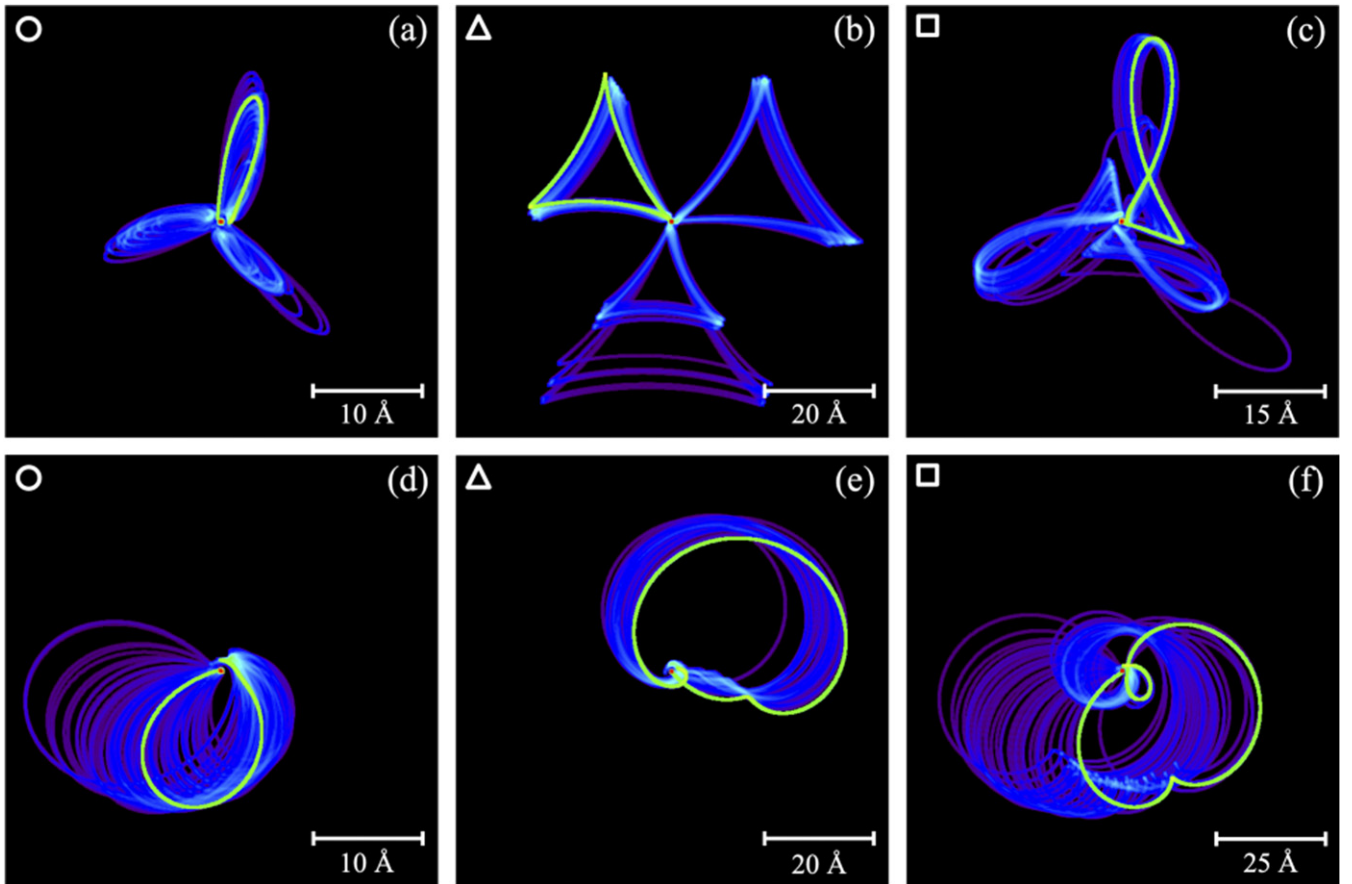

Figure 12. Ensembles of 100 electron trajectories are shown as a heat map for various parameters as indicated by the circle, triangle and square in figure 11. In (a)–(c) counterrotating fields, trajectories can take on (a) short, looping shapes, (b) triangular shapes similar to the simpleman closed-loop paths, and (c) hybrid fish-shaped trajectories composed of both loops and triangles. For (d)–(f) corotating fields, the patterns are all looping cycloid shapes, with size scales determined by the rescattering timing. A single sample trajectory is highlighted for each case, and the color scale is optimized to highlight the trajectories in each plot.

ionization. While there is not a direct correlation between ionization pathway and electron momentum, it is clear how different mechanisms contribute to the different portions of the electron momentum distribution.

The differentiation between these processes is even more compelling in the corotating case, shown in figure 10 for a $\beta = 3.0$ pulse (same as in figure 8(i)). As with the counterrotating case, the electrons involved in impact ionization, shown
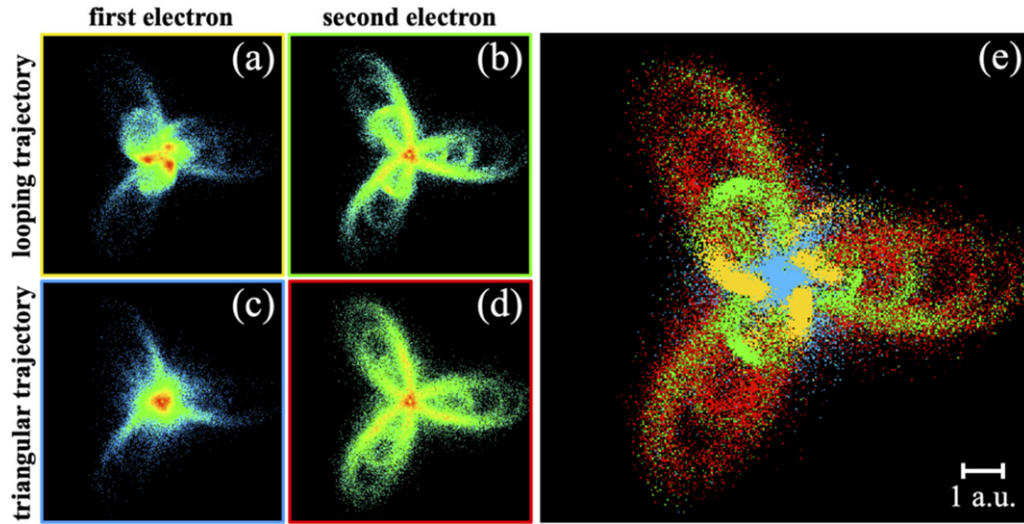
Figure 13. Transverse electron momenta are shown for a $\beta = 2.0$ counterrotating pulse at 1×10^{16} W cm^{-2} (as in figure 8(e)). The distributions from the (a) first electron and the (b) second electron from looping trajectories (rescattering time less than 1.8 fs), and the (c) first electron and the (d) second electron from triangular trajectories are shown. Contributions from these four patterns are color coded and (e) combined into a single image. This figure is the result of 1.2×10^8 simulation runs, the color scale spans three orders of magnitude (for (a)–(d)), and the scale is displayed in atomic units.

in figures 10(a) and (b), have relatively low, spread-out energies, and the first electron contributing to excitation ionization (figure 10(c)) is peaked near zero momentum. But since the field-ionized electrons will take on the pattern of the vector potential at the peak of the electric field, this portion of the distribution is well separated to high momenta (figure 10(d)), as expected from the energy spectra shown in figure 7(f).

The composite pattern, shown in figure 10(e), shows rather well-distinguished regions corresponding to the first and second electron contributing to either impact or excitation ionization, and confirms that the high-energy structure observed in figure 7(f) is in fact due to electrons released through impact excitation followed by field ionization.

4.6. Rescattering timing and electron trajectories

In order to appreciate the types of electron trajectories that contribute to double-ionization events, it is useful to examine the rescattering timing for various pulse conditions. The rescattering time as a function of ellipticity (for single-color pulses) or field amplitude ratio (for bicircular fields) is shown in figure 11, and is defined as the time between the instant an electron gains positive total energy and its subsequent time of nearest return to the ion. In figure 12, ensembles of 100 rescattering electron trajectories are shown for specific amplitude ratios and timing, as indicated in the timing plots.

For single-color pulses, shown in figure 11(a), double ionization peaks for rescattering times slightly shorter than one-half of an optical cycle. This corresponds to the familiar case of an electron released after the peak in the electric field amplitude and returning after the next peak. Multiple returns are also possible, but become less likely with increasing ellipticity.

For counterrotating fields, shown in figure 11(b), the evolution of the rescattering timing with changing field amplitude

ratio takes on an interesting pattern. While a very quick trajectory is possible for a range of amplitude ratios, it is peaked for $\beta \approx 1$ and corresponds to a nearly 'out-and-back' looping trajectory (see figure 12(a)). Multiple returns are also possible for a range of ratios, but are most likely for $\beta \approx 2$, where a closed-loop (and potentially repeating) triangular trajectory is common (see figure 12(b)). For other regions in the timing heat map, the trajectories transition between looping and triangular patterns, exhibiting shapes such as the 'fish' trajectory shown in figure 12(c). In fact, all of the possible trajectories that contribute to double ionization with counterrotating pulses are comprised of a combination of looping and triangular shapes, where the proportion of looping and triangular portions will vary depending on field amplitude ratio and rescattering time.

For corotating fields, as shown in figure 11(c), very short returns are possible, but the dominant process is due to longer (but still sub-cycle) trajectories across a broad range of field amplitude ratios. In all cases, the trajectories exhibit looping shapes, as expected from the shapes of the simpleman trajectories shown in figure 1.

To determine the effect of the different trajectories on the resulting electron momentum distributions, we again analyze the pattern from a $\beta = 2.0$ counterrotating pulse (same as in figure 8(e)). This time we differentiate between the first and second electron involved in a looping trajectory (rescattering time less than 1.8 fs) and the first and second electron involved in a triangular trajectory (rescattering time greater than 1.8 fs).

The momentum distribution for the first liberated electron from a looping trajectory (figure 13(a)) exhibits three peaks away from the origin, while the first electron from a triangular trajectory (figure 13(c)) has a momentum centered at zero. This indicates that looping trajectories bring the electron back with appreciable kinetic energy, resulting in the three peaks of

J. Phys. B: At. Mol. Opt. Phys. **53** (2020) 185601

J L Chaloupka

non-zero momentum. But the closed-loop, full-cycle triangular trajectories return the electron with nearly zero kinetic energy, resulting in low electron momenta (and also supporting multiple returns, since the electron is back to where it started a full cycle later). The momentum patterns from the second electron from looping (figure 13(b)) or triangular (figure 13(d)) trajectories are quite similar, showing only subtle differences related to the timing of the first, returning electron. The composite image shown in figure 13(e) is generated in the same way as in figure 9, and shows how the two types of electron trajectories contribute to the total electron momentum distribution.

5. Conclusions

We have presented results from classical ensemble simulations of the single and double ionization of helium in intense bicircular laser fields. The electron energy spectra from single ionization show clear indications of scattering off of the ion core, even for corotating fields where returning trajectories are unlikely. Electron momentum distributions in the transverse plane show clear and measurable effects of electron delay from the interaction with the Coulomb potential for elliptical and bicircular fields. NSDI is found to occur for a wide range of field amplitude ratios for both counter- and co-rotating pulses, and the yield, electron energy and momentum, and rescattering timing have been mapped out in detail. The contributions to the electron momentum patterns from the first and second electron involved in impact or excitation ionization show how structure in these distributions can be attributed to different ionization pathways. For counterrotating fields, looping and triangular rescattering trajectories contribute to different portions of the resulting electron momentum distribution.

While this study has been limited to the ionization of helium with intense 2ω:ω pulses, the methodologies applied here could be easily utilized with higher-Z atoms (by modifying the ionic potential [48]), molecules (by altering the Hamiltonian [58]), and pulses composed of other colors or polarizations. This work provides insight into how bicircular fields could be used to probe atomic or molecular structure [59, 60] through photoelectron [61, 62] or high-harmonic [63, 64] spectroscopy, in particular making use of trajectories with very different electron release and impact angles (e.g., the fish-shaped trajectory in figure 12(c)). Ongoing studies at different intensities, pulse widths, and wavelengths will be performed to explore the diversity of rescattering dynamics with bicircular fields.

ORCID iDs

Jan L Chaloupka ⬥ https://orcid.org/0000-0002-2978-1336

References

[1] Voronov G S and Delone N B 1966 *Sov. Phys - JETP* **23** 54
[2] L'Huillier A, Lompre L A, Mainfray G and Manus C 1983 *Phys. Rev.* A **27** 2503
[3] Fittinghoff D N, Bolton P R, Chang B and Kulander K C 1992 *Phys. Rev. Lett.* **69** 2642
[4] Walker B, Sheehy B, DiMauro L F, Agostini P, Schafer K J and Kulander K C 1994 *Phys. Rev. Lett.* **73** 1227
[5] Kuchiev M Y 1987 *JETP Lett.* **45** 404
[6] Corkum P B 1993 *Phys. Rev. Lett.* **71** 1994
[7] Schafer K J, Yang B, DiMauro L F and Kulander K C 1993 *Phys. Rev. Lett.* **70** 1599
[8] Becker W, Liu X, Ho P J and Eberly J H 2012 *Rev. Mod. Phys.* **84** 1011
[9] Lafon R, Chaloupka J L, Sheehy B, Paul P M, Agostini P, Kulander K C and DiMauro L F 2001 *Phys. Rev. Lett.* **86** 2762
[10] Rudenko A, de Jesus V L B, Ergler T, Zrost K, Feuerstein B, Schröter C D, Moshammer R and Ullrich J 2007 *Phys. Rev. Lett.* **99** 263003
[11] McPherson A, Gibson G, Jara H, Johann U, Luk T S, McIntyre I A, Boyer K and Rhodes C K 1987 *J. Opt. Soc. Am.* B **4** 595
[12] Ferray M, L'Huillier A, Li X F, Lompre L A, Mainfray G and Manus C 1988 *J. Phys. B: At. Mol. Opt. Phys.* **21** L31
[13] Lewenstein M, Balcou P, Ivanov M Y, L'Huillier A and Corkum P B 1994 *Phys. Rev.* A **49** 2117
[14] Dietrich P, Burnett N, Ivanov M and Corkum P B 1994 *Phys. Rev.* A **50** R3585
[15] Eichmann H, Egbert A, Nolte S, Momma C, Wellegehausen B, Becker W, Long S and McIver J K 1995 *Phys. Rev.* A **51** R3414
[16] Milošević D B, Becker W and Kopold R 2000 *Phys. Rev.* A **61** 063403
[17] Kramo A, Hasović E, Milošević D B and Becker W 2007 *Laser Phys. Lett.* **4** 279
[18] Fleischer A, Kfir O, Diskin T, Sidorenko P and Cohen O 2014 *Nat. Photon.* **8** 543
[19] Mancuso C A *et al* 2015 *Phys. Rev.* A **91** 031402
[20] Odžak S and Milošević D B 2015 *Phys. Rev.* A **92** 053416
[21] Kfir O *et al* 2015 *Nat. Photon.* **9** 99
[22] Hickstein D D *et al* 2015 *Nat. Photon.* **9** 743
[23] Fan T *et al* 2015 *Proc. Natl Acad. Sci. USA* **112** 14206
[24] Mancuso C A *et al* 2016 *Phys. Rev.* A **93** 053406
[25] Milošević D B and Becker W 2016 *Phys. Rev.* A **93** 063418
[26] Hasović E, Becker W and Milošević D B 2016 *Opt. Express* **24** 6413
[27] Baykusheva D, Ahsan M S, Lin N and Wörner H J 2016 *Phys. Rev. Lett.* **116** 123001
[28] Eckart S *et al* 2016 *Phys. Rev. Lett.* **117** 133202
[29] Odžak S, Hasović E, Becker W and Milošević D B 2017 *J. Mod. Opt.* **64** 971
[30] Lin K *et al* 2017 *Phys. Rev. Lett.* **119** 203202
[31] Ben S, Guo P Y, Pan X F, Xu T T, Song K L and Liu X S 2017 *Chem. Phys. Lett.* **679** 38
[32] Eckart S *et al* 2018 *Phys. Rev.* A **97** 041402(R)
[33] Ma X, Zhou Y, Chen Y, Li M, Li Y, Zhang Q and Lu P 2019 *Opt. Express* **27** 1825
[34] Chaloupka J L and Hickstein D D 2016 *Phys. Rev. Lett.* **116** 143005
[35] Mancuso C A *et al* 2016 *Phys. Rev. Lett.* **117** 133201
[36] Ben S, Zuo W, Song K, Xu T, Guo J, Xu H, Yan B and Liu X-S 2016 *Opt. Commun.* **380** 462
[37] Mancuso C A, Dorney K M, Hickstein D D, Chaloupka J L, Tong X-M, Ellis J L, Kapteyn H C and Murnane M M 2017 *Phys. Rev.* A **96** 023402
[38] Huang C, Zhong M and Wu Z 2018 *Opt. Express* **26** 26045
[39] Huang C, Zhong M and Wu Z 2019 *Opt. Express* **27** 7616

J. Phys. B: At. Mol. Opt. Phys. **53** (2020) 185601

J L Chaloupka

[40] Bauer D 1997 *Phys. Rev.* A **56** 3028
[41] Panfili R, Haan S L and Eberly J H 2002 *Phys. Rev. Lett.* **89** 113001
[42] Ho P, Panfili R, Haan S L and Eberly J H 2005 *Phys. Rev. Lett.* **94** 093002
[43] Haan S L, Breen L, Karim A and Eberly J H 2006 *Phys. Rev. Lett.* **97** 103008
[44] Haan S L, Van Dyke J S and Smith Z S 2008 *Phys. Rev. Lett.* **101** 113001
[45] Paquette J P and Chaloupka J L 2009 *Phys. Rev.* A **79** 043410
[46] Wang X and Eberly J H 2012 *Phys. Rev.* A **86** 013421
[47] Li Y-B, Wang X, Yu B-H, Tang Q-B, Wang G-H and Wan J-G 2016 *Sci. Rep.* **6** 37413
[48] Wang X 2013 *PhD Thesis* University of Rochester
[49] Linden v d, Heuvell H B v and Muller H G 1988 *Multi-Photon Processes Studies in Modern Optics* vol 8 (Cambridge: Cambridge University Press) p 25
[50] Gallagher T F 1988 *Phys. Rev. Lett.* **61** 2304
[51] Corkum P B, Burnett N H and Brunel F 1989 *Phys. Rev. Lett.* **62** 1259
[52] Krausz F and Ivanov M 2009 *Rev. Mod. Phys.* **81** 163
[53] Walker B, Sheehy B, Kulander K C and DiMauro L F 1996 *Phys. Rev. Lett.* **77** 5031
[54] Eckle P, Smolarski M, Schlup P, Biegert J, Staudte A, Schöffler M, Muller H G, Dörner R and Keller U 2008 *Nat. Phys.* **4** 565
[55] Eckle P, Pfeiffer A N, Cirelli C, Staudte A, Dörner R, Muller H G, Büttiker M and Keller U 2008 *Science* **5** 1525
[56] Pfeiffer A N, Cirelli C, Smolarski M, Dörner R and Keller U 2011 *Nat. Phys.* **7** 428
[57] Sainadh U S *et al* 2019 *Nature* **568** 75
[58] Huang C, Zhou Y, Tong A, Liao Q, Hong W and Lu P 2011 *Opt. Express* **19** 5627
[59] Abu-samha M and Madsen L B 2018 *J. Phys. B: At. Mol. Opt. Phys.* **51** 135401
[60] Ke Q, Zhou Y, Tan J, He M, Liang J, Zhao Y, Li M and Lu P 2019 *Opt. Express* **27** 32193
[61] Blaga C I, Xu J, DiChiara A D, Sistrunk E, Zhang K, Agostini P, Miller T A, DiMauro L F and Lin C D 2012 *Nature* **483** 194
[62] Xu J, Blaga C I, Zhang K, Lai Y H, Lin C D, Miller T A, Agostini P and DiMauro L F 2014 *Nat. Commun.* **5** 4635
[63] Li W, Zhou X, Lock R, Patchkovskii S, Stolow A, Kapteyn H C and Murnane M M 2008 *Science* **322** 1207
[64] Jin C, Bertrand J B, Lucchese R R, Wörner H J, Corkum P B, Villeneuve D M, Le A-T and Lin C D 2012 *Phys. Rev.* A **85** 013405